

Revealing the chemical structure of the Class I disc Oph-IRS 67

E. Artur de la Villarmois¹, L. E. Kristensen¹, and J. K. Jørgensen¹

Niels Bohr Institute & Centre for Star and Planet Formation, University of Copenhagen, Øster Voldgade 5–7, 1350 Copenhagen K., Denmark
e-mail: elizabeth.artur@nbi.ku.dk

January 19, 2022

ABSTRACT

Context. Recent results suggest that the first steps towards planet formation may be already taking place in protoplanetary discs during the first 100,000 years after stars form. It is therefore crucial to unravel the physical and chemical structures of such discs in their earliest stages while they are still embedded in their natal envelopes and compare them with more evolved systems.

Aims. The purpose of this paper is to explore the structure of a line-rich Class I protobinary source, Oph-IRS 67, and analyse the differences and similarities with Class 0 and Class II sources.

Methods. We present a systematic molecular line study of IRS 67 with the Submillimeter Array (SMA) on 1–2'' (150–300 AU) scales. The wide instantaneous band-width of the SMA observations (~30 GHz) provide detections of a range of molecular transitions that trace different physics, such as CO isotopologues, sulphur-bearing species, deuterated species, and carbon-chain molecules.

Results. We see significant differences between different groups of species. For example, the CO isotopologues and sulphur-bearing species show a rotational profile and are tracing the larger-scale circumbinary disc structure, while CN, DCN, and carbon-chain molecules peak at the southern edge of the disc at blue-shifted velocities. In addition, the cold gas tracer DCO⁺ is seen beyond the extent of the circumbinary disc.

Conclusions. The detected molecular transitions can be grouped into three main components: cold regions far from the system, the circumbinary disc, and a UV-irradiated region likely associated with the surface layers of the disc that are reached by the UV radiation from the sources. The different components are consistent with the temperature structure derived from the ratio of two H₂CO transitions, that is, warm temperatures are seen towards the outflow direction, lukewarm temperatures are associated with the UV-radiated region, and cold temperatures are related with the circumbinary disc structure. The chemistry towards IRS 67 shares similarities with both Class 0 and Class II sources, possibly due to the high gas column density and the strong UV radiation arising from the binary system. IRS 67 is, therefore, highlighting the intermediate chemistry between deeply embedded sources and T-Tauri discs.

Key words. ISM: molecules – stars: formation – protoplanetary discs – astrochemistry – ISM: individual objects: Oph-IRS 67

1. Introduction

Protoplanetary discs are a crucial stage between warm cores and the formation of planetesimals and planets, and the final composition of planets likely depends on the chemical processing within the disc. The chemical complexity of the disc is established by the material that is incorporated from the inner envelope and by physical processes that promotes a chemical reset (e.g. outflows, accretion shocks, UV radiation field; Bergin et al. 2003; Ceccarelli 2004; Herbst & van Dishoeck 2009; Sakai & Yamamoto 2013; Miura et al. 2017). The detail of how and when the disc forms are still not well understood. In particular, the physics and chemistry of the innermost regions are challenging to observe and study, as they are embedded within a large amount of gas and dust. It is, therefore, essential to study and understand the first stages of discs formation. This paper presents an extensive Submillimeter Array (SMA) survey of the molecular line emission on a few hundred AU scales towards the Class I protobinary system Oph-IRS 67, and investigates the physical and chemical signatures associated with the system.

The complex structure of embedded discs is associated with a huge range of temperatures (~10–1000 K) and densities (10⁵–10¹³ cm⁻³; Herbst & van Dishoeck 2009; van Dishoeck 2018), making molecules excellent diagnostics of the physical conditions and processes. Chemical surveys towards deeply em-

bedded sources show the potential of the chemistry to shed light on the physical structure of these regions (e.g. Jørgensen et al. 2016; Lefloch et al. 2018; Yoshida et al. 2019). Also, the chemical inventories and initial conditions of young discs can then be compared with discs around more evolved (Class II or T Tauri) young stars (e.g. Öberg et al. 2011; Kastner et al. 2018).

Class I discs represent the bridge between deeply embedded Class 0 sources and the emergence of planet-forming discs, that is, Class II sources. Recent high-sensitivity and spatial resolution observations suggest that planet formation starts at early stages (Class I), based on the evidence of considerable grain growth (e.g. ALMA Partnership et al. 2015; Harsono et al. 2018). The study of Class I discs is, therefore, essential in order to constrain the first steps of planet formation and to analyse the chemical evolution of discs at different stages. The observations of Class I discs are challenging since they are small in size (~100 AU; Harsono et al. 2014; Yen et al. 2015) and other components, such as inner envelope and outflow material, can contribute to the emission on small scales.

The Class I protobinary system IRS 67 is located in the Ophiuchus star forming region and belongs to the L1689 cloud. It has been associated with a large-scale outflow structure (≥1000 AU; Bontemps et al. 1996), bolometric temperature (T_{bol}) of 130 K, and bolometric luminosity (L_{bol}) of 4.0 L_☉ (Dunham et al. 2015).

The binarity of the system was proven by McClure et al. (2010) at infrared wavelengths, where a separation of $0''.6$ (~ 90 AU for a distance of 151.2 pc; Ortiz-León et al. 2017) was found between the sources. More recently, a Keplerian circumbinary disc has been associated to IRS 67 with an extent of ~ 620 AU (Artur de la Villarmois et al. 2018). In comparison with other Class I sources, IRS 67 shows a particular rich chemistry and bright emission of $c\text{-C}_3\text{H}_2$ (Artur de la Villarmois et al. 2018, 2019), a molecule commonly associated with photon-dominated regions (PDRs; Guzmán et al. 2015; Murillo et al. 2018).

This paper presents an SMA chemical survey towards the Class I proto-binary system IRS 67 and is laid out as follows. Section 2 presents the observational details, data calibration, and spectral coverage. The continuum emission, detected molecular transitions, contour maps, moment 0 maps, and spectral features are described in Sect. 3. We discuss the chemical and physical structure of IRS 67 in Sect. 4, together with an analysis of the non-detected molecular lines, and a comparison with other stages of low-mass star formation. Finally, the main results are summarised in Sect. 5.

2. Observations

We observed IRS 67 using the Submillimeter Array (SMA), in the extended and compact configurations on 2017 February 24 and 2017 April 21, respectively (program code: 2016B-S0004; PI: Elizabeth Artur de la Villarmois). The antenna configuration provided projected baselines between 10 and 188 metres. A pointing centre of $\alpha = 16^{\text{h}}32^{\text{m}}00^{\text{s}}.98$, $\delta = -24^{\circ}56'43''.4$ (J2000) was used, corresponding to the peak of the continuum emission at 0.87 mm (Artur de la Villarmois et al. 2018). The observations covered a frequency range of ~ 30 GHz, between 214.3 and 245.6 GHz (Table 1) with a spectral resolution of 139.64 kHz (0.18 km s^{-1}).

The calibration and imaging were done in CASA¹ (McMullin et al. 2007). For the extended track, the complex gains were calibrated through observations of the quasar 1626-298, passband calibration on 3c273, and flux calibration on Ganymede. For the compact track, the gain, passband, and flux calibrations were implemented by observing the quasar 1626-298, 3c454.3, and Callisto, respectively. The extended and compact observations were combined and a Briggs weighting with robustness parameter of 1 was applied to the visibilities. The resulting dataset has a typical beam size of $1''.7 \times 1''.4$ ($\sim 260 \times 210$ AU) and a maximum angular scale of $\sim 25''$. The continuum and line *rms* are given in Table 1.

3. Results

3.1. Continuum

The continuum emission for each receiver and sideband is fitted with two-dimensional (2D) Gaussians in the image plane, and the resulting deconvolved size, position angle, integrated flux, and intensity peak are listed in Table 2. The continuum emission at 0.87 mm, previously detected with ALMA (Artur de la Villarmois et al. 2018), showed the contribution of both protostellar sources and a circumbinary disc, associated with a position angle of 54° , an extent of ~ 620 AU, and a total integrated flux (both sources and disc) of 0.30 Jy.

In the Rayleigh-Jeans limit of the spectrum, the submillimeter flux (F_ν) has a power-law dependence with the frequency, i.e. $F_\nu \propto \nu^\alpha$, where α is the slope of the sub-mm spectral

energy distribution (SED) and is related with the dust opacity spectral index (β) by $\alpha = \beta + 2$ (e.g. Beckwith & Sargent 1991; Testi et al. 2014). By fitting a power law distribution to the integrated fluxes from Table 2 and the 0.87 mm value from Artur de la Villarmois et al. (2018), an α index of 2.8 ± 0.3 is found, and $\beta = 0.8 \pm 0.3$. The typical β -value of the interstellar medium (ISM) is ~ 1.7 (Natta et al. 2007), therefore, a lower value suggests grain growth or optically thick dust emission. This is consistent with the results from Jørgensen et al. (2007), who find an α index of between two and three for a sample of Class 0 protostars.

3.2. Molecular transitions

The observations covered multiple molecular transitions, such as CO isotopologues, S-bearing species, deuterated species, and carbon-chain molecules. The detected transitions are listed in Table 3 with their spectroscopic parameters, while the lines without detection above a 3σ level are listed in Table B.1 in the Appendix.

3.2.1. CO isotopologues

The CO emission is shown in Fig. 1 for different velocity ranges. Most of the CO emission is expected to be extended and thus, filtered out by the interferometer due to the lack of short spacings. By comparing APEX data (Lindberg et al. 2017) with convolved SMA C^{18}O emission (see Fig. C.1 and Table C.1 in the Appendix), the recovered C^{18}O flux with the SMA is less than 1%. Since CO is the more abundant isotopologue, and its emission is expected to be more extended than C^{18}O , the filtering out of emission is more significant for CO and thus, the recovered CO flux is expected to be much lower than 1%. This implies that the SMA observations are probing the deepest and denser regions, and the detected CO emission in Fig. 1 traces the more compact structures. The emission is centred at the position of the system, probing outer-envelope material, and knot-like structures are detected in red-shifted emission between 1 and 2 km s^{-1} and blue-shifted emission between 3 and 4 km s^{-1} , which are consistent with the outflow direction found by Bontemps et al. (1996) (see upper-left panel of Fig. 1).

Emission from ^{13}CO , C^{18}O , and C^{17}O is shown in Fig. 2. ^{13}CO presents a flatted shape that follows the circumbinary disc structure and extends beyond it. C^{18}O follows a similar distribution as ^{13}CO , and C^{17}O stands out towards the southern part of the disc. Another C^{17}O transition ($J=3-2$) is analysed by Artur de la Villarmois et al. (2018), where the emission traces the Keplerian circumbinary disc, therefore, the differences seen between $\text{C}^{17}\text{O } J=3-2$ and $\text{C}^{17}\text{O } J=2-1$ may be related to the sensitivity of the observations. A rotational profile, perpendicular to the outflow direction, is clearly seen for ^{13}CO and C^{18}O for velocities beyond $\pm 2 \text{ km s}^{-1}$.

3.2.2. Sulphur-bearing species

Emission of CS and the brightest SO transition (6_5-5_4) is also shown in Fig. 2. The high dipole moment of CS makes this molecule a very good high-density tracer (e.g. van der Tak et al. 2000). Its emission shows a large extent ($\sim 10''$) and peaks at the edges of the circumbinary disc, showing a rotational profile around the binary system. SO shows a more compact distribution than CS, tracing the circumbinary disc material. SO 6_5-5_4 is slightly brighter than SO 5_5-4_4 (see Fig. A.1 in the Appendix)

¹ <http://casa.nrao.edu/>

Table 1. Summary of the observations.

Receiver	Sideband	Frequency range (GHz)	Continuum <i>rms</i> (Jy beam ⁻¹)	Spectral <i>rms</i> (Jy beam ⁻¹ channel) ^(a)
230	lower	214.3 - 222.3	0.001	0.08
240	lower	221.6 - 229.6	0.003	0.15
230	upper	230.3 - 238.3	0.001	0.10
240	upper	237.6 - 245.6	0.004	0.17

Notes. ^(a) The channel width is 0.18 km s⁻¹.

Table 2. Results of 2D Gaussian fits towards the continuum peaks.

Receiver	Sideband	Size ^(a) ($''$)	PA ($^{\circ}$)	Integrated flux (Jy)	Intensity peak (Jy beam ⁻¹)
230	lower	$1.4 \pm 0.1 \times 0.7 \pm 0.2$	38 ± 9	0.087 ± 0.004	0.056 ± 0.002
240	lower	$1.4 \pm 0.2 \times 1.0 \pm 0.4$	3 ± 44	0.097 ± 0.007	0.064 ± 0.003
230	upper	$1.2 \pm 0.1 \times 0.6 \pm 0.1$	41 ± 6	0.105 ± 0.003	0.071 ± 0.002
240	upper	$1.6 \pm 0.3 \times 1.3 \pm 0.5$	24 ± 81	0.130 ± 0.012	0.068 ± 0.005

Notes. ^(a) Deconvolved size (FWHM).

and a third SO transition (1_2-2_1) was also targeted, however, no emission is detected above a 3σ level. This may be related with its low A_{ij} , which is two orders of magnitude lower than the value from the detected SO transitions (see Tables 3 and B.1 in the Appendix).

Less abundant CS isotopologues, such as C³⁴S and ¹³CS, are shown in Fig. A.2 in the Appendix, where C³⁴S is more than a factor of two brighter than ¹³CS, in agreement with their relative abundances with respect to CS (³²S/³⁴S=22 and ¹²C/¹³C=69; Wilson 1999). C³⁴S follows the CS emission, where both species peak at the edges of the circumbinary disc. ¹³CS, on the other hand, presents isolated peaks that lack a clear correlation with the main isotopologue. The emission does, however, have a low signal-to-noise level ($\leq 4\sigma$).

3.2.3. H₂CO

The observations include six H₂CO transitions, associated with E_u values from 21 to 280 K. The transitions with the highest E_u (174 and 280 K) are not detected (see Table B.1) and the strongest lines are o-H₂CO $3_{1,2}-2_{1,1}$ ($E_u = 33$ K) and p-H₂CO $3_{0,3}-2_{0,2}$ ($E_u = 21$ K), shown in Fig. 2. The emission extends beyond the circumbinary disc structure, peaks towards the edges of the disc, and the intensity decreases towards the positions of the protostars. This is similar to what is seen for CS, however, the H₂CO emission stands out towards the southern part of the circumbinary disc and the peak is slightly south from the disc. It is interesting to notice that the southern part of the disc is related with blue-shifted emission, while the blue component of the outflow is seen towards the north-west.

Two H₂CO transitions ($3_{2,2}-2_{2,1}$ and $3_{2,1}-2_{2,0}$) show weak emission and are presented in Fig. A.2 in the Appendix. Their emission do not follow the distribution from the brightest H₂CO transition ($3_{1,2}-2_{1,1}$), however, both of them are associated with higher E_u values of 68 K. As previously shown (e.g. Mangum & Wootten 1993), and further discussed in Section 4.1, the intensity ratios of these specific H₂CO transitions are sensitive tracers of the gas kinetic temperature and density.

3.2.4. Carbon-chain molecules

The C₃H₂ molecule has two isomeric forms: cyclic (c-C₃H₂) and linear (l-C₃H₂). Although standard astrochemical models predict a cyclic-to-linear C₃H₂ ratio of ~ 1 , observations show higher values ranging from 3 to 70 (Sipilä et al. 2016). Our observations targeted nine c-C₃H₂ transitions, with E_u between 19 and 87 K, and three l-C₃H₂ transitions, with E_u between 66 and 80 K (see Tables 3 and B.1). However, the linear isomer is not detected. Figure 2 shows the brightest c-C₃H₂ transition, where the emission stands out between -3 and -1 km s⁻¹ and peaks south from the circumbinary disc. Other three c-C₃H₂ lines present weaker emission and are shown in Fig. A.3 in the Appendix.

The brightest c-C₃H₂ transition ($6_{0,6}-5_{1,5}$) was also detected with APEX by Lindberg et al. (2017) (see Appendix), and more than 92% of the flux is filtered out by the interferometer, suggesting that the c-C₃H₂ distribution is much more extended than what is seen in Fig. 2. In addition, c-C₃H₂ is the only transition in the APEX data that peaks at 2.9 km s⁻¹, and not at 4.2 km s⁻¹ like the rest of the detected molecular transitions (DCO⁺, H₂CO, C¹⁸O, and SO). The velocity of 2.9 km s⁻¹ is consistent with the blue-shifted material detected in the SMA observations, where the c-C₃H₂ emission stands out between -3 and -1 km s⁻¹ with respect to the binary system velocity.

Three HC₃N transitions are detected and shown in Fig. A.3 in the Appendix. The emission peaks south of the circumbinary disc, which is consistent with the c-C₃H₂ emission, suggesting that this region is rich in carbon-chain molecules. On the other hand, the HC₃N $J=24-23$ transition was observed with APEX, but not detected, therefore, the emission may arise from a compact component (i.e. the emission is suffering from beam dilution).

3.2.5. CN

CN is known as a photon-dominated region (or photodissociation region, PDR) tracer, since its abundance increases when HCN photo-dissociates into CN due to ultraviolet (UV) radiation from the star or the interstellar radiation field (Willacy & Langer 2000; Aikawa & Herbst 2001; van Zadelhoff et al. 2003). Although gas-phase CN is expected to be abundant towards protostars, it is often challenging to observe with interferometers at millimeter

Table 3. Parameters of the detected molecular transitions.

Species	Transition	Frequency ^(a) (GHz)	A_{ij} ^(a) (s ⁻¹)	E_u ^(a) (K)	n_{crit} ^(b) (cm ⁻³)
CO- species					
CO	$J=2-1$	230.53800	6.92×10^{-7}	17	2.2×10^4
¹³ CO	$J=2-1$	220.39868	6.07×10^{-7}	16	2.0×10^4
C ¹⁸ O	$J=2-1$	219.56035	6.01×10^{-7}	16	1.9×10^4
C ¹⁷ O	$J=2-1$	224.71439	6.42×10^{-7}	16	2.1×10^4
H ₂ CO	$3_{0,3}-2_{0,2}$ (para)	218.22219	2.82×10^{-4}	21	3.4×10^6
H ₂ CO	$3_{2,2}-2_{2,1}$ (para)	218.47563	1.58×10^{-4}	68	1.4×10^6
H ₂ CO	$3_{2,1}-2_{2,0}$ (para)	218.76007	1.58×10^{-4}	68	3.2×10^6
H ₂ CO	$3_{1,2}-2_{1,1}$ (ortho)	225.69778	2.75×10^{-4}	33	5.7×10^6
Deuterated species					
DCO ⁺	$J=3-2$	216.11258	2.38×10^{-3}	21	7.0×10^6
DCN	$3-2$	217.23854	4.57×10^{-4}	21	2.5×10^7
DNC	$3-2$	228.91049	5.62×10^{-4}	22	4.9×10^6
S- species					
CS	$5-4$	244.93556	2.95×10^{-4}	35	8.7×10^6
C ³⁴ S	$5-4$	241.01609	2.75×10^{-4}	28	8.0×10^6
¹³ CS	$5-4$	231.22069	2.51×10^{-4}	33	7.4×10^6
SO	5_5-4_4	215.22065	1.20×10^{-4}	44	1.8×10^8 ^(c)
SO	6_5-5_4	219.94944	1.35×10^{-4}	35	2.5×10^8 ^(c)
N- species					
CN ^(d)	$N=2-1, J=3/2-3/2, F=1/2-1/2$	226.28742	1.02×10^{-5}	16	6.1×10^4
CN	$N=2-1, J=3/2-3/2, F=5/2-5/2$	226.35987	1.62×10^{-5}	16	5.8×10^5
CN	$N=2-1, J=3/2-1/2, F=1/2-3/2$	226.61657	1.07×10^{-5}	16	1.8×10^5
CN	$N=2-1, J=3/2-1/2, F=3/2-3/2$	226.63219	4.27×10^{-5}	16	2.6×10^5
CN	$N=2-1, J=3/2-1/2, F=5/2-3/2$	226.65956	9.55×10^{-5}	16	7.0×10^5
CN	$N=2-1, J=3/2-1/2, F=1/2-1/2$	226.66369	8.51×10^{-5}	16	6.0×10^5
CN	$N=2-1, J=3/2-1/2, F=3/2-1/2$	226.67931	5.25×10^{-5}	16	3.8×10^5
CN	$N=2-1, J=5/2-3/2, F=5/2-3/2$	226.87419	9.55×10^{-5}	16	2.4×10^6
CN	$N=2-1, J=5/2-3/2, F=7/2-5/2$	226.87478	1.15×10^{-4}	16	5.1×10^7
CN	$N=2-1, J=5/2-3/2, F=3/2-1/2$	226.87590	8.51×10^{-5}	16	1.2×10^6
CN	$N=2-1, J=5/2-3/2, F=3/2-3/2$	226.88742	2.75×10^{-5}	16	9.5×10^5
CN	$N=2-1, J=5/2-3/2, F=5/2-5/2$	226.89213	1.82×10^{-5}	16	5.4×10^5
¹³ CN	$N=2-1, J=5/2-3/2, F=4-3$	217.46715	1.01×10^{-4}	16	
Carbon-chain species					
c-C ₃ H ₂	$3_{3,0}-2_{2,1}$ (ortho)	216.27876	2.57×10^{-4}	19	2.0×10^8
c-C ₃ H ₂	$6_{0,6}-5_{1,5}$ (para)	217.82215	5.37×10^{-4}	39	8.7×10^7
c-C ₃ H ₂	$5_{1,4}-4_{2,3}$ (ortho)	217.94005	3.98×10^{-4}	35	6.3×10^7
c-C ₃ H ₂	$5_{2,4}-4_{1,3}$ (para)	218.16046	4.07×10^{-4}	35	9.0×10^7
c-C ₃ H ₂	$7_{2,6}-7_{1,7}$ (para)	218.73273	8.91×10^{-5}	61	2.9×10^7
c-C ₃ H ₂	$4_{3,2}-3_{2,1}$ (ortho)	227.16914	3.09×10^{-4}	29	2.8×10^7
HC ₃ N	$J=24-23$	218.32472	8.32×10^{-4}	131	4.7×10^7
HC ₃ N	$J=25-24$	227.41891	9.33×10^{-4}	142	1.2×10^7
HC ₃ N	$J=26-25$	236.51279	1.05×10^{-3}	153	3.2×10^7

Notes. ^(a) Values from the CDMS database (Müller et al. 2001). ^(b) Calculated values for a collisional temperature of 30 K and collisional rates from the Leiden Atomic and Molecular Database (LAMDA; Schöier et al. 2005). ^(c) For a collisional temperature of 60 K. ^(d) CN transitions with A_{ij} higher than $1 \times 10^{-5} \text{ s}^{-1}$. The references for collisional rates of specific species are presented in Table B.1.

wavelengths as it typically is extended and filtered out (e.g. Jørgensen et al. 2011). Towards one Class 0 source, L483-mm, CN was found to probe material in the boundary between the bulk protostellar envelope and its outflow cavity (Jørgensen 2004). CN has also been detected towards a number of protostellar discs around Class II sources (e.g. Dutrey et al. 1997; Qi 2001; Thi et al. 2004; Öberg et al. 2011), where it is found to be a good tracer of the disc surfaces (e.g. van Dishoeck 2006).

Toward IRS67, ten of the twelve hyperfine transitions from CN 2–1 (see Table 3) are detected. The emission of one of these hyperfine transitions is shown in Fig. 3. The brightest CN lines are blended with other CN hyperfine transitions and their moment 0 maps are shown in Fig. A.4 in the Appendix. The CN emission stands out towards the southern region and peaks slightly offset from the southern edge of the circumbinary disc, which is consistent with the H₂CO peak (see Fig. 2).

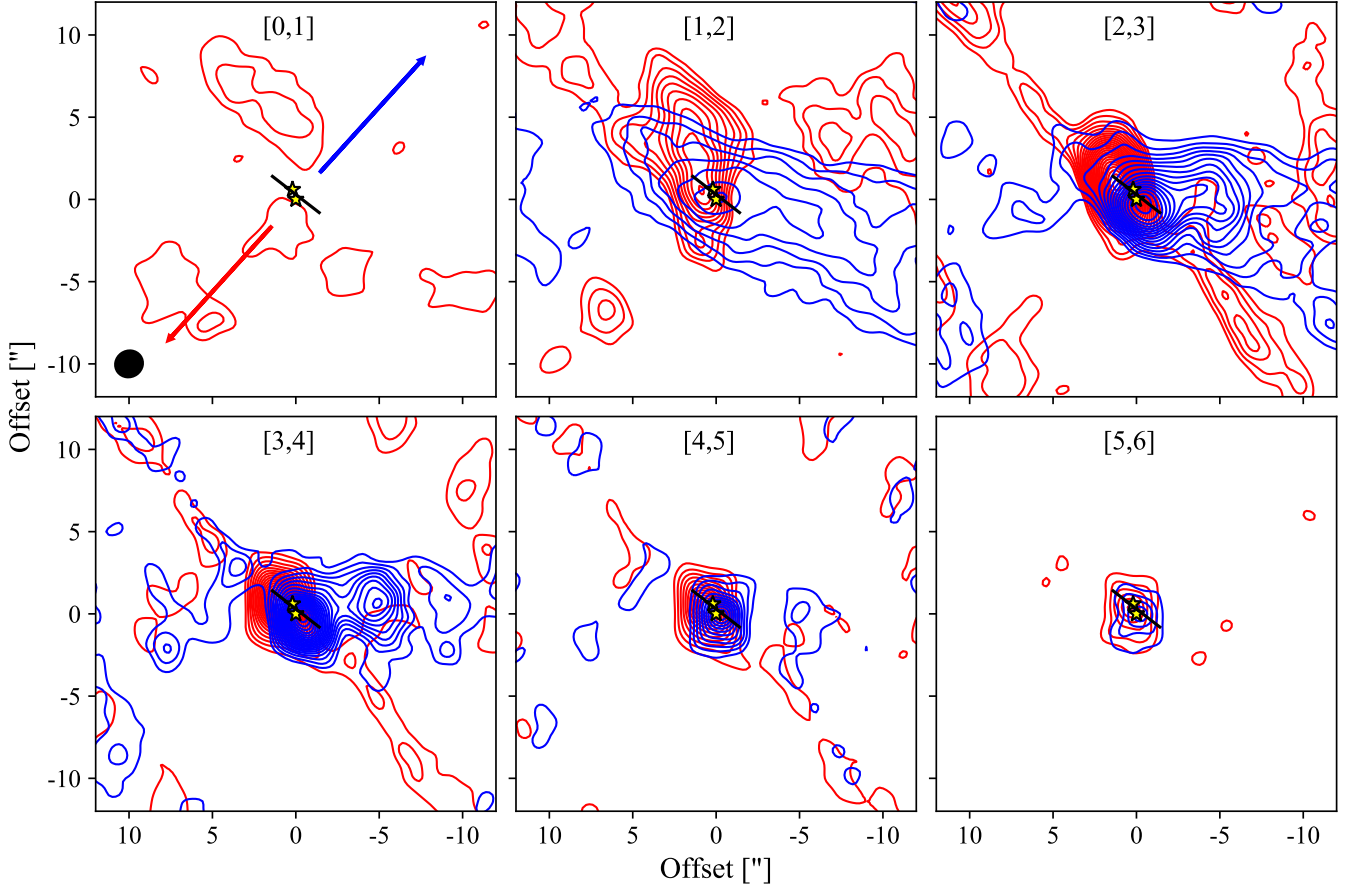


Fig. 1. CO emission above 5σ ($\sigma = 0.04 \text{ Jy beam}^{-1} \text{ km s}^{-1}$). The contours start at 5σ and follow a step of 5σ . The numbers in brackets indicate the velocity interval in units of km s^{-1} and the extent of the circumbinary disc is represented by the black solid segment. The yellow stars show the position of the sources. The synthesised beam and the outflow direction from Bontemps et al. (1996) are represented in the upper-left panel with a black filled ellipse and blue and red arrows, respectively.

3.2.6. Deuterated species

Deuterated species are good tracers of cold regions, in particular, the outer disc midplane where the temperature is $\leq 30 \text{ K}$ (e.g. van Dishoeck 2006; Jørgensen et al. 2011; Murillo et al. 2015; Öberg et al. 2015; Aikawa et al. 2018). The ion DCO^+ is apparently formed in the gas phase, considering its short destruction timescale and is expected to be abundant in regions with temperature between 19 and 21 K (Aikawa et al. 2018). On the other hand, neutral species as DCN can form in interstellar ice and later desorb in the disc, thus tracing regions with higher temperatures than DCO^+ ($\geq 30 \text{ K}$; Jørgensen et al. 2004; Aikawa et al. 2018). Emission of DCN, DNC, and DCO^+ is detected and shown in Fig. 3. Both DCN and DNC peak towards the southern edge of the protobinary disc, which is consistent with the CN peak, while DCO^+ stands out close to the northern edge of the disc and no emission is detected where DCN and DNC peak.

3.2.7. Spectra

Figure 4 shows the spectra of the species presented in Figs. 2 and 3, towards three different positions: the geometric centre and the blue- and red-shifted peaks from the CS emission, located at $2''$ and $2.4''$ from the geometric centre, respectively (see white crosses in the moment 0 map of CS in Fig. 2). CO and ^{13}CO show a clear absorption feature at the system velocity (4.2 km s^{-1}), mainly due to the interferometric filtering-out of emission from

large scales. C^{18}O , CS, SO, and the two brightest H_2CO transitions present similar spectral features, with prominent emission between -3 and 3 km s^{-1} and a considerably symmetry between the blue- and red-shifted components. These components are tracing the edges of the circumbinary disc, peak around $\pm 2 \text{ km s}^{-1}$ and are consistent with a rotational profile. This is in agreement with the results from Artur de la Villarmois et al. (2018), where velocities below $\pm 2.5 \text{ km s}^{-1}$ are expected at a distance of $2''$ from the geometric centre and beyond. On the other hand, $\text{c-C}_3\text{H}_2$, DCN, DNC, and HC_3N show strong emission towards the southern edge of the circumstellar disc (blue spectra), with a peak around -2 km s^{-1} , tracing a different component than the CO isotopologues, CS, SO and H_2CO .

Since the observations include multiple CN hyperfine transitions, their spectra are shown in Fig. 5, covering a frequency range from 226.356 to 226.896 GHz. The spectra of isolated lines show an absorption feature at the system velocity, consistent with filtering-out of emission from large scales. This agrees with the results from Jørgensen et al. (2011), where the CN emission may be tracing the outer envelope towards IRAS 16293-2422 and is filtered out by the SMA. Nevertheless, towards IRS 67 the CN emission peaks at the southern edge of the circumbinary disc, with velocities around -2 km s^{-1} . The CN spectra resemble that of $\text{c-C}_3\text{H}_2$ (Fig. 4), suggesting that the two species trace the same material.

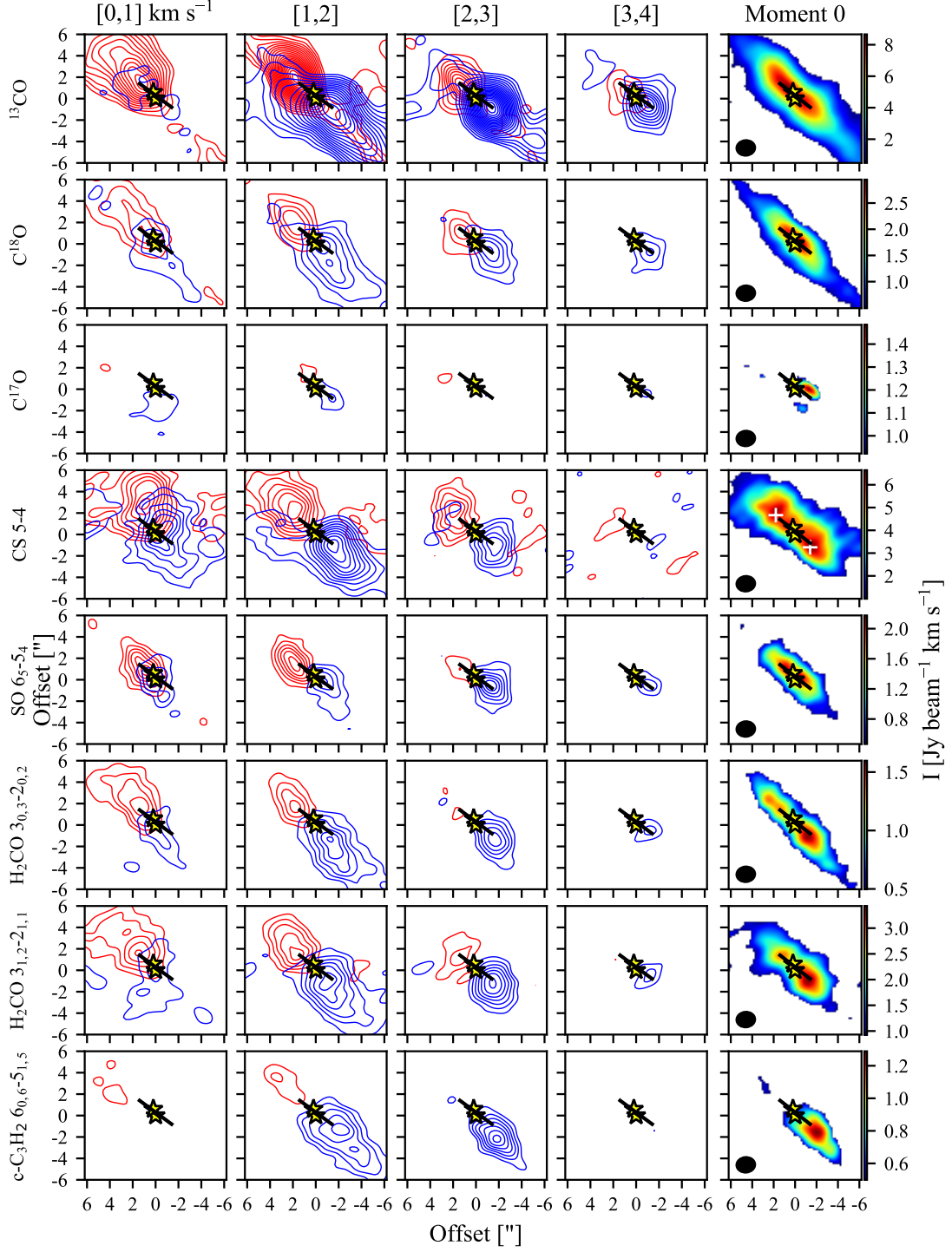


Fig. 2. Emission of CO isotopologues and other bright molecular transitions. Channel maps consist of velocity ranges of 1 km s^{-1} and moment 0 maps are integrated over a velocity range of 8 km s^{-1} . The contours start at 5σ and follow a step of 5σ for ^{13}CO , C^{18}O , and CS (the remaining follow a step of 3σ). The two white crosses in the CS moment 0 map indicate the position from which the spectra from Figs. 4 and 5 are extracted. The yellow stars show the position of the sources and the solid segment represents the extent of the circumbinary disc. The synthesised beam is represented by a solid black ellipse in the right panels.

4. Discussion

4.1. Structure of IRS 67

The ratio between $\text{H}_2\text{CO } 3_{0,3}-2_{0,2}$ and $\text{H}_2\text{CO } 3_{2,2}-2_{2,1}$ has previously been shown to be a good tracer of the gas temperature

(Mangum & Wootten 1993). Figure 6 shows the estimated gas temperature for a H_2 number density $\geq 10^8 \text{ cm}^{-3}$, following those results. The highest temperatures ($\geq 90 \text{ K}$) are seen towards the outflow direction, while the southern edge of the circumbinary disc is associated with temperatures between 50 and 60 K.

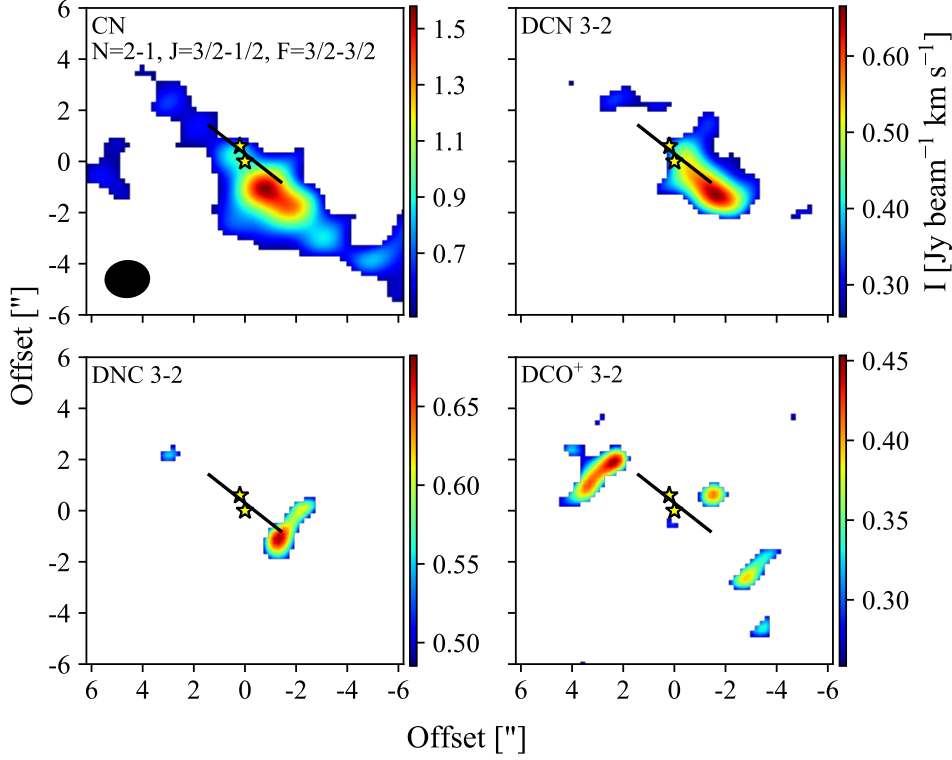


Fig. 3. CN and deuterated species, DCN, DNC, and DCO^+ , moment 0 maps integrated over a velocity range of 6 km s^{-1} . The yellow stars show the position of the sources and the solid segment represents the extent of the circumbinary disc. The synthesised beam is represented by a black filled ellipse in the upper-left panel.

This is the region where the peak of emission is seen for DCN, DNC, CN, $\text{c-C}_3\text{H}_2$, and HC_3N , suggesting that these species are tracing high densities ($n_{\text{H}_2} \geq 10^8 \text{ cm}^{-3}$) and lukewarm temperatures (50–60 K). The non-detection of $\text{H}_2\text{CO } 3_{2,2}-2_{2,1}$ where $\text{H}_2\text{CO } 3_{0,3}-2_{0,2}$ is detected sets an upper limit of 50 K for the gas temperature (the grey region in Fig. 6).

CN and $\text{c-C}_3\text{H}_2$ are commonly used as PDR tracers, since their emission shows a strong dependence on the UV radiation (e.g. Dutrey et al. 1997; van Dishoeck 2006; Öberg et al. 2011; Bergin et al. 2016; Murillo et al. 2018). The circumbinary disc associated with IRS 67 may be strongly illuminated by UV radiation from the binary system. Because discs are normally flared, is it also likely that the southern region of the circumbinary disc is associated with a PDR, in particular, the surface layer of the circumbinary disc. Other common PDRs originate along the outflow cavity (e.g. Murillo et al. 2018), however, this is unlikely for IRS 67 since the blue-shifted outflow component is seen towards the north-west, and blue-shifted emission from $\text{c-C}_3\text{H}_2$ is detected towards the south-east. The PDR originating at the surface layer of the circumbinary disc is also consistent with the temperature structure estimated from the $\text{H}_2\text{CO } 3_{0,3}-2_{0,2}/3_{2,2}-2_{2,1}$ ratio (see Fig. 6).

The northern part of the circumbinary disc seems to be related with colder regions than the southern part (see Fig. 6). DCO^+ is expected to trace cold regions ($\leq 30 \text{ K}$; Jørgensen et al. 2011; Aikawa et al. 2018) and its emission peaks towards the north-east of the circumbinary disc (Fig. 3), showing an anti-correlation with the PDR tracers (mainly CN and $\text{c-C}_3\text{H}_2$). The DCO^+ emission seems to be associated with cold regions from the inner envelope at small scales ($\leq 1000 \text{ AU}$), however, the same DCO^+ transition was detected with APEX (see Fig. C.1

in the Appendix), suggesting that more than 96% of the emission is filtered out by the interferometer. Therefore, DCO^+ is expected to be present also at large scales (e.g. Jørgensen et al. 2011; Murillo et al. 2018).

The system IRS 67 is particularly rich in molecular lines when it is compared with other single Class I sources (Artur de la Villarmois et al. 2019), possibly due to the mass content and extent of the circumbinary disc. One of the species that is only detected towards IRS 67, among other 11 Class I sources, is $\text{c-C}_3\text{H}_2$, where two transitions ($5_{5,1}-4_{4,0}$ and $5_{5,0}-4_{4,1}$) are seen (Artur de la Villarmois et al. 2018) and the emission is consistent with the $\text{c-C}_3\text{H}_2$ lines analysed in this work. $\text{c-C}_3\text{H}_2$ may, therefore, be related with PDRs (like outflow cavities and disc surface layers) but also with high gas column densities expected towards Class 0 sources and the binary system IRS 67. This is in agreement with the non-detection of $\text{c-C}_3\text{H}_2$ towards a sample of 12 Class II discs (Öberg et al. 2010, 2011).

4.2. Non-detections

Together with the detection of multiple molecular transitions, the non-detections may provide some clues about the physical parameters of the region. The main non-detections at the 3σ level are N_2D^+ , the linear isomer $\text{l-C}_3\text{H}_2$, SiO, and CH_3OH .

N_2D^+ is a good tracer of cold regions ($\leq 30 \text{ K}$), where CO freezes out, and usually correlates with DCO^+ (e.g. Jørgensen et al. 2011; Aikawa et al. 2018; Murillo et al. 2018). Since most of the DCO^+ is filtered out by the interferometer and its emission is expected to be present at large scales, N_2D^+ may also be present at large scales. Therefore, the non-detection of N_2D^+ may be related to the lack of short-spacings in the observations.

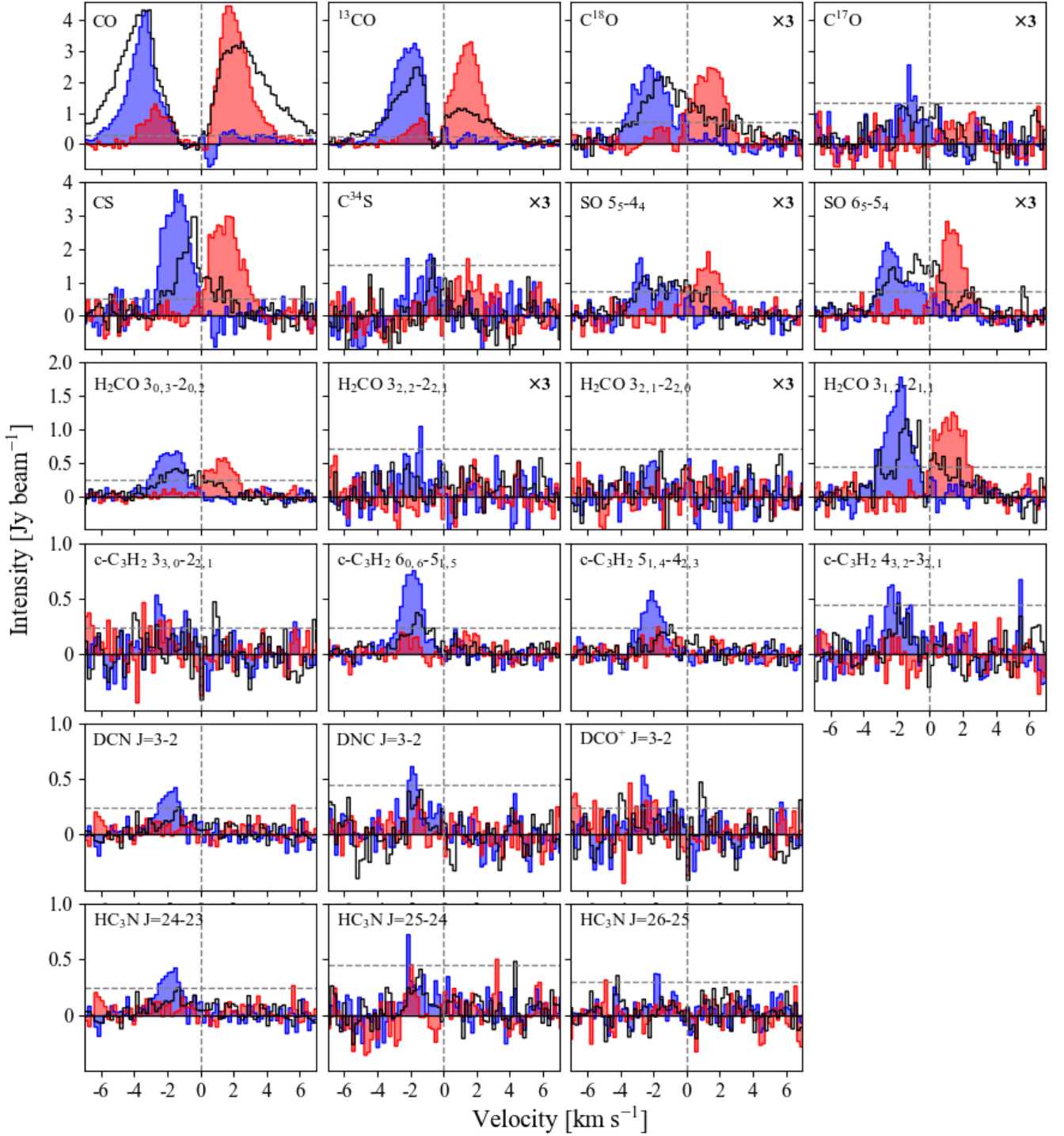


Fig. 4. Spectra of the brightest molecular transitions (with the exception of CN) taken at three different positions: the geometric centre (black), the southern edge (blue), and the northern edge of the circumbinary disc (red; see the white crosses in the moment 0 map of CS in Fig. 2). The zero velocity value (dashed grey vertical line) corresponds to a system velocity of 4.2 km s^{-1} . The dashed grey horizontal line shows the value of 3σ (see Table 1). Some of the spectra are multiplied by a factor of three, as indicated in the top right corner.

The non-detection of the linear C_3H_2 isomer may be related with the high cyclic-to-linear ratio or to an excitation effect, or a combination of both. The cyclic-to-linear ratio has been proven to differ from the statistical value of one for a variety of objects, ranging from 3 to 70 (Sipilä et al. 2016). On the other hand, the three l- C_3H_2 transitions covered in the observations have E_u val-

ues between 66 and 80 K, while the brightest c- C_3H_2 line (see Fig. 2) has $E_u = 39 \text{ K}$. In addition, c- C_3H_2 $7_{2,6}-7_{1,7}$ ($E_u = 61 \text{ K}$) shows weak emission and two c- C_3H_2 lines with $E_u = 87 \text{ K}$ are not detected. This sets an upper limit of 60 K for the excitation temperature of the c- C_3H_2 emitting region. Therefore, a combi-

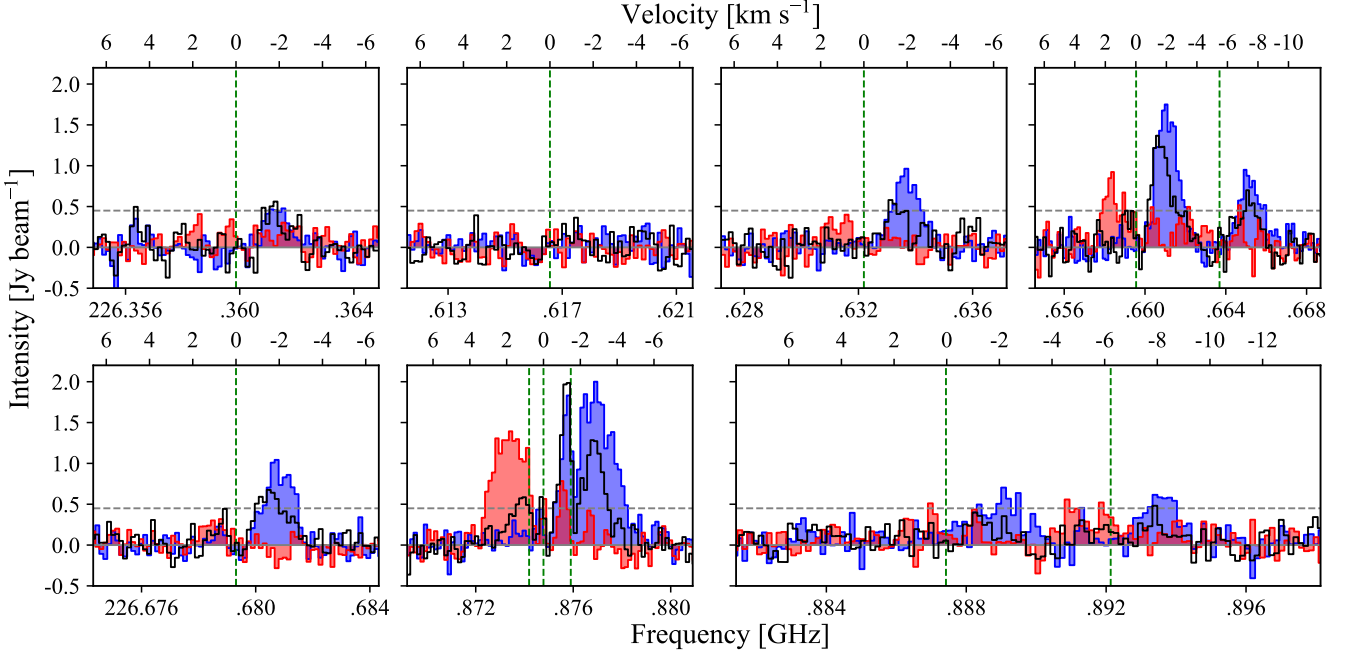


Fig. 5. CN spectra taken at three different positions: the geometric centre (black), the southern edge (blue), and the northern edge of the circumbinary disc (red; see white crosses in the moment 0 map of CS in Fig. 2). The dashed green vertical lines represent the rest frequency of the CN hyperfine transitions (see Table 3), while the dashed grey horizontal line shows the value of 3σ .

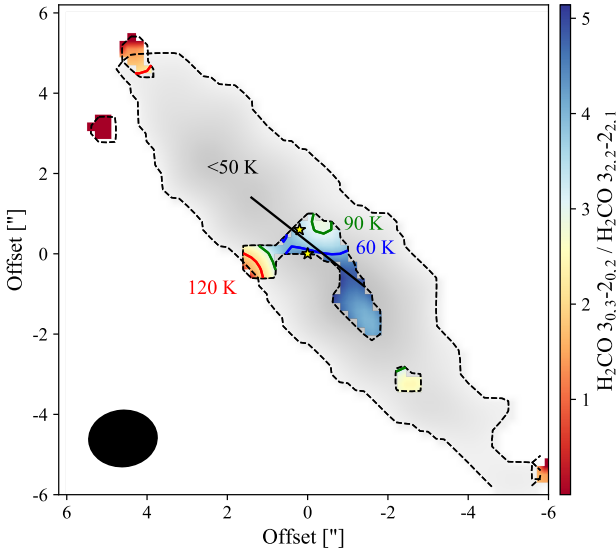


Fig. 6. Gas temperature estimation from the ratio between $\text{o-H}_2\text{CO } 3_{0,3}-2_{0,2}$ and $\text{o-H}_2\text{CO } 3_{2,2}-2_{2,1}$, following the results from Mangum & Wootten (1993). Specific values of 60, 90, and 120 K are shown by blue, green, and red contours, respectively. The grey region, where $\text{o-H}_2\text{CO } 3_{2,2}-2_{2,1}$ is not detected, indicates temperatures below 50 K. The yellow stars show the position of the sources and the solid segment represents the extent of the circumbinary disc. The synthesised beam is represented by a black filled ellipse.

nation of both, high cyclic-to-linear ratio and an excitation effect, may explain the non detection of the linear C_3H_2 isomer.

Typically, SiO is seen as a good tracer of shocks as it is present in the gas-phase when refractory grains are destroyed (e.g. Bachiller & Perez Gutierrez 1997; Codella et al. 2014; Gusdorf et al. 2008b,a). Its non-detection towards IRS 67 is consis-

tent with other studies which suggest that Class I sources are associated with less energetic outflows.

4.3. Chemical differentiation around IRS 67

Figure 7 shows a schematic representation of the environment associated with IRS 67, where three main regions are distinguished: (i) a cold region ($T \leq 30$ K) beyond the extent of the circumbinary disc, traced by DCO^+ , (ii) the circumbinary disc traced by CO isotopologues and sulphur-bearing species, and (iii) a PDR, likely the surface layer of the circumbinary disc reached by the UV radiation from the binary system, and traced by CN, DCN, and carbon-chain molecules.

The chemistry towards IRS 67 shows some similarities with Class 0 sources, possibly due to the high-gas column density, and with Class II discs, where the UV radiation from the binary system may resemble the interaction between a typical T-Tauri star and the surface layers of its disc. Cold gas tracers (such as DCO^+ and DCN), potential grain chemistry products (such as H_2CO), and species associated with carbon-chain chemistry (such as $\text{c-C}_3\text{H}_2$ and HC_3N), are commonly detected towards Class 0 sources (e.g. Jørgensen et al. 2005; Murillo et al. 2018) and are also detected towards IRS 67. However, while H_2CO and $\text{c-C}_3\text{H}_2$ are mainly seen at the outflow cavities towards Class 0 sources, towards IRS 67 they seem to trace the surface layers of the circumbinary disc. On the other hand, photochemistry products such as CN are abundant towards more evolved discs, associated with Class II sources (e.g. Öberg et al. 2010, 2011): CN will originate in the outer, very low density part of the disc, which is completely exposed to UV radiation. The binary system IRS 67 may be associated with a stronger UV radiation field than single Class I sources, therefore, the CN emission towards IRS 67 appears to trace the same physical component as in Class II sources, that is, the surface layers of the disc exposed to UV radiation. Future observations of other Class I binary sources will

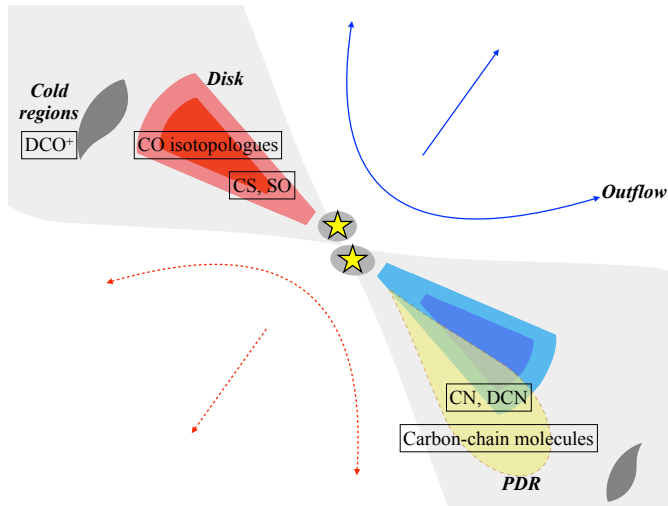


Fig. 7. Schematic representation of the environment towards IRS 67 where three main regions are distinguished. Cold regions traced by DCO^+ , the disc structure proven by CO isotopologues and S-bearing species, and a PDR associated with the surface layers of the disc, traced by CN, DCN, and carbon-chain molecules. The outflow direction is taken from Bontemps et al. (1996).

verify whether the chemical richness of IRS 67 is common towards these stages, and higher angular resolutions will constrain the velocity profile and the dynamics of the detected transitions.

5. Summary

This work presents SMA observations of the Class I binary system IRS 67 in the Ophiuchus star forming region, with an angular resolution of $1''.7 \times 1''.4$ ($\sim 260 \times 210$ AU). The continuum emission between 1.2 and 1.4 mm is analysed, together with multiple molecular transitions that trace different physics. The main results are summarised below.

- The continuum emission is consistent with previous studies (Artur de la Villarmois et al. 2018) and a power-law fitting results in a β -value of 0.8 ± 0.3 , suggesting that dust grains have grown to larger sizes than the ISM dust particles, or that the dust is optically thick.
- The detected molecular transitions are tracing three main regions: cold regions beyond the circumbinary disc extent, the circumbinary disc, and a PDR likely related with the surface layers of the disc. DCO^+ is tracing the cold regions, while the CO isotopologues and the sulphur-bearing species are probing the disc structure. In addition, CN, DCN, and carbon-chain molecules are tracing the PDR.
- The case of H_2CO is special, as it traces both the circumbinary disc and the PDR. The ratio between $\text{o-H}_2\text{CO } 3_{0,3}-2_{0,2}$ and $\text{o-H}_2\text{CO } 3_{2,2}-2_{2,1}$ has been shown to be a good indicator of the gas temperature, where the temperature map is consistent with the physical structure of IRS 67, that is, the warmer gas follows the outflow direction, lukewarm temperatures are associated with the PDR, and colder gas is related to the circumbinary disc.
- IRS 67 shows chemical similarities with Class 0 sources, such as the detection of sulphur-bearing species and carbon-chain molecules, while PDR tracers, such as CN, are associated with Class II discs, where the UV radiation can reach the surface layers of the disc. IRS 67 is, therefore, a chemical link between these two stages.

This work shows the potential of the broad spectral coverage of the SMA, allowing us to detect and analyse multiple molecules and transitions from the same species. Similar observations of other Class I sources will provide more statistical results and highlight if IRS 67 is a particular chemically-rich system or it represents a general trend. In addition, higher angular resolution observations will constrain the dynamics of the gas and possibly resolve the individual circumstellar discs around each source, constraining the link between circumstellar and circumbinary discs.

Acknowledgements. We thank Johan Lindberg for sharing and discussing APEX data with us. This paper is based on data from the Submillimeter Array: the Submillimeter Array is a joint project between the Smithsonian Astrophysical Observatory and the Academia Sinica Institute of Astronomy and Astrophysics, and is funded by the Smithsonian Institution and the Academia Sinica. The group of JKJ acknowledges support from the European Research Council (ERC) under the European Union’s Horizon 2020 research and innovation programme (grant agreement No 646908) through ERC Consolidator Grant “S4F”. Research at the Centre for Star and Planet Formation is funded by the Danish National Research Foundation.

Appendix A: Other molecular transitions

Other transitions and less abundant isotopologues of the species discussed in Sect. 3.2 show weaker emission and are presented in Figs. A.1, A.2, and A.3. In addition, the brightest CN hyperfine transitions are blended with other CN lines (see Fig. 5). Emission of these transitions is shown in Fig. A.4.

Appendix B: Non-detections

Non-detected lines at the 3σ level within the covered molecular transitions are listed in Table B.1, along with their spectroscopic parameters.

Appendix C: APEX data

The system IRS 67 was observed with APEX (Lindberg et al. 2017) around 220 GHz and with an angular resolution of $29''$. In order to compare SMA with APEX data, the SMA observations are convolved with a $29''$ beam and the intensity unit (Jy beam^{-1}) is converted into Kelvin. Figure C.1 shows a comparison between the two datasets for five transitions, highlighting the strong filtering-out of extended emission by the interferometer. The APEX and SMA intensities are presented in Table C.1, together with the percentage of emission that has been filtered out.

References

- Aikawa, Y., Furuya, K., Hincelin, U., & Herbst, E. 2018, *ApJ*, 855, 119
Aikawa, Y. & Herbst, E. 2001, *A&A*, 371, 1107
ALMA Partnership, Brogan, C. L., Pérez, L. M., et al. 2015, *ApJ*, 808, L3
Artur de la Villarmois, E., Jørgensen, J. K., Kristensen, L. E., et al. 2019, *arXiv e-prints*, arXiv:1904.13161
Artur de la Villarmois, E., Kristensen, L. E., Jørgensen, J. K., et al. 2018, *A&A*, 614, A26
Bachiller, R. & Perez Gutierrez, M. 1997, in *IAU Symposium*, Vol. 182, Herbig-Haro Flows and the Birth of Stars, ed. B. Reipurth & C. Bertout, 153–162
Balança, C., Spielfiedel, A., & Feautrier, N. 2016, *MNRAS*, 460, 3766
Beckwith, S. V. W. & Sargent, A. I. 1991, *ApJ*, 381, 250
Bergin, E., Calvet, N., D'Alessio, P., & Herczeg, G. J. 2003, *ApJ*, 591, L159
Bergin, E. A., Du, F., Cleaves, L. I., et al. 2016, *ApJ*, 831, 101
Bontemps, S., Andre, P., Terebey, S., & Cabrit, S. 1996, *A&A*, 311, 858
Ceccarelli, C. 2004, in *Astronomical Society of the Pacific Conference Series*, Vol. 323, Star Formation in the Interstellar Medium: In Honor of David Hollenbach, ed. D. Johnstone, F. C. Adams, D. N. C. Lin, D. A. Neufeld, & E. C. Ostriker, 195
Chandra, S. & Kegel, W. H. 2000, *A&AS*, 142, 113
Codella, C., Maury, A. J., Gueth, F., et al. 2014, *A&A*, 563, L3
Daniel, F., Dubernet, M.-L., & Grosjean, A. 2011, *A&A*, 536, A76
Dayou, F. & Balança, C. 2006, *A&A*, 459, 297
Dumouchel, F., Faure, A., & Lique, F. 2010, *MNRAS*, 406, 2488
Dunham, M. M., Allen, L. E., Evans, II, N. J., et al. 2015, *ApJS*, 220, 11
Dutrey, A., Guilloteau, S., & Bachiller, R. 1997, *A&A*, 325, 758
Faure, A., Lique, F., & Wiesenfeld, L. 2016, *MNRAS*, 460, 2103
Faure, A., Wiesenfeld, L., Scribano, Y., & Ceccarelli, C. 2012, *MNRAS*, 420, 699
Flower, D. R. 1999, *MNRAS*, 305, 651
Green, S. & Chapman, S. 1978, *ApJS*, 37, 169
Gusdorf, A., Cabrit, S., Flower, D. R., & Pineau Des Forêts, G. 2008a, *A&A*, 482, 809
Gusdorf, A., Pineau Des Forêts, G., Cabrit, S., & Flower, D. R. 2008b, *A&A*, 490, 695
Guzmán, V. V., Pety, J., Goicoechea, J. R., et al. 2015, *ApJ*, 800, L33
Harsono, D., Bjerkeli, P., van der Wiel, M. H. D., et al. 2018, *Nature Astronomy*, 2, 646
Harsono, D., Jørgensen, J. K., van Dishoeck, E. F., et al. 2014, *A&A*, 562, A77
Herbst, E. & van Dishoeck, E. F. 2009, *ARA&A*, 47, 427
Jørgensen, J. K. 2004, *A&A*, 424, 589
Jørgensen, J. K., Bourke, T. L., Myers, P. C., et al. 2007, *ApJ*, 659, 479
Jørgensen, J. K., Bourke, T. L., Nguyen Luong, Q., & Takakuwa, S. 2011, *A&A*, 534, A100
Jørgensen, J. K., Schöier, F. L., & van Dishoeck, E. F. 2004, *A&A*, 416, 603
Jørgensen, J. K., Schöier, F. L., & van Dishoeck, E. F. 2005, *A&A*, 437, 501
Jørgensen, J. K., van der Wiel, M. H. D., Coutens, A., et al. 2016, *A&A*, 595, A117
Kalugina, Y. & Lique, F. 2015, *MNRAS*, 446, L21
Kastner, J. H., Qi, C., Dickson-Vandervelde, D. A., et al. 2018, *ApJ*, 863, 106
Lefloch, B., Bachiller, R., Ceccarelli, C., et al. 2018, *MNRAS*, 477, 4792
Lindberg, J. E., Charnley, S. B., Jørgensen, J. K., Cordiner, M. A., & Bjerkeli, P. 2017, *ApJ*, 835, 3
Lique, F., Spielfiedel, A., & Cernicharo, J. 2006, *A&A*, 451, 1125
Mangum, J. G. & Wootten, A. 1993, *ApJS*, 89, 123
McClure, M. K., Furlan, E., Manoj, P., et al. 2010, *ApJS*, 188, 75
McMullin, J. P., Waters, B., Schiebel, D., Young, W., & Golap, K. 2007, in *Astronomical Society of the Pacific Conference Series*, Vol. 376, *Astronomical Data Analysis Software and Systems XVI*, ed. R. A. Shaw, F. Hill, & D. J. Bell, 127
Miura, H., Yamamoto, T., Nomura, H., et al. 2017, *ApJ*, 839, 47
Müller, H. S. P., Thorwirth, S., Roth, D. A., & Winnewisser, G. 2001, *A&A*, 370, L49
Murillo, N. M., Bruderer, S., van Dishoeck, E. F., et al. 2015, *A&A*, 579, A114
Murillo, N. M., van Dishoeck, E. F., van der Wiel, M. H. D., et al. 2018, *A&A*, 617, A120
Natta, A., Testi, L., Calvet, N., et al. 2007, *Protostars and Planets V*, 767
Öberg, K. I., Furuya, K., Loomis, R., et al. 2015, *ApJ*, 810, 112
Öberg, K. I., Qi, C., Fogel, J. K. J., et al. 2010, *ApJ*, 720, 480
Öberg, K. I., Qi, C., Fogel, J. K. J., et al. 2011, *ApJ*, 734, 98
Ortiz-León, G. N., Loinard, L., Kounkel, M. A., et al. 2017, *ApJ*, 834, 141
Qi, C. 2001, PhD thesis, CALIFORNIA INSTITUTE OF TECHNOLOGY
Rabli, D. & Flower, D. R. 2010, *MNRAS*, 406, 95
Sahnoun, E., Wiesenfeld, L., Hammami, K., & Jaidane, N. 2018, *The Journal of Physical Chemistry A*, 122, 3004
Sakai, N. & Yamamoto, S. 2013, *Chemical Reviews*, 113, 8981
Schöier, F. L., van der Tak, F. F. S., van Dishoeck, E. F., & Black, J. H. 2005, *A&A*, 432, 369
Sipilä, O., Spezzano, S., & Caselli, P. 2016, *A&A*, 591, L1
Testi, L., Birnstiel, T., Ricci, L., et al. 2014, *Protostars and Planets VI*, 339
Thi, W.-F., van Zadelhoff, G.-J., & van Dishoeck, E. F. 2004, *A&A*, 425, 955
van der Tak, F. F. S., van Dishoeck, E. F., Evans, II, N. J., & Blake, G. A. 2000, *ApJ*, 537, 283
van Dishoeck, E. F. 2006, *Proceedings of the National Academy of Science*, 103, 12249
van Dishoeck, E. F. 2018, in *IAU Symposium*, Vol. 332, *IAU Symposium*, ed. M. Cunningham, T. Millar, & Y. Aikawa, 3–22
van Zadelhoff, G.-J., Aikawa, Y., Hogerheijde, M. R., & van Dishoeck, E. F. 2003, *A&A*, 397, 789
Wiesenfeld, L. & Faure, A. 2013, *MNRAS*, 432, 2573
Willacy, K. & Langer, W. D. 2000, *ApJ*, 544, 903
Wilson, T. L. 1999, *Reports on Progress in Physics*, 62, 143
Yang, B., Stancil, P. C., Balakrishnan, N., & Forrey, R. C. 2010, *ApJ*, 718, 1062
Yen, H.-W., Koch, P. M., Takakuwa, S., et al. 2015, *ApJ*, 799, 193
Yoshida, K., Sakai, N., Nishimura, Y., et al. 2019, *PASJ[arXiv:1901.06546]*

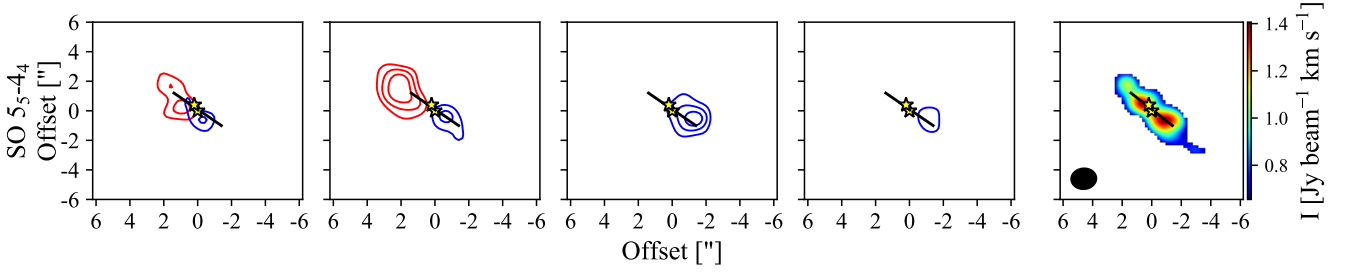


Fig. A.1. Emission of SO 5_5-4_4 . Channel maps consist of velocity ranges of 1 km s^{-1} and the moment 0 map is integrated over a velocity range of 8 km s^{-1} . The contours start at 3σ and follow a step of 3σ . The yellow stars show the position of the sources and the solid segment represents the extent of the circumbinary disc. The synthesised beam is represented in the right panel by a solid black ellipse.

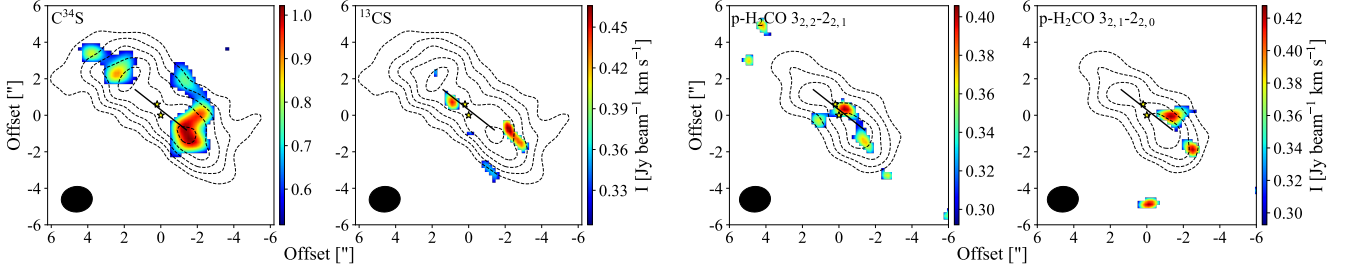


Fig. A.2. C^{34}S , ^{13}CS , and H_2CO ($E_u = 68 \text{ K}$) moment 0 maps (colour scale) integrated over a velocity range of 6 km s^{-1} , overlapped with CS emission (contours in C^{34}S and ^{13}CS maps) and H_2CO $3_{1,2}-2_{1,1}$ (contours in H_2CO maps) from Fig. 2. The yellow stars show the position of the sources and the solid segment represents the extent of the circumbinary disc. The synthesised beam is represented by a black filled ellipse.

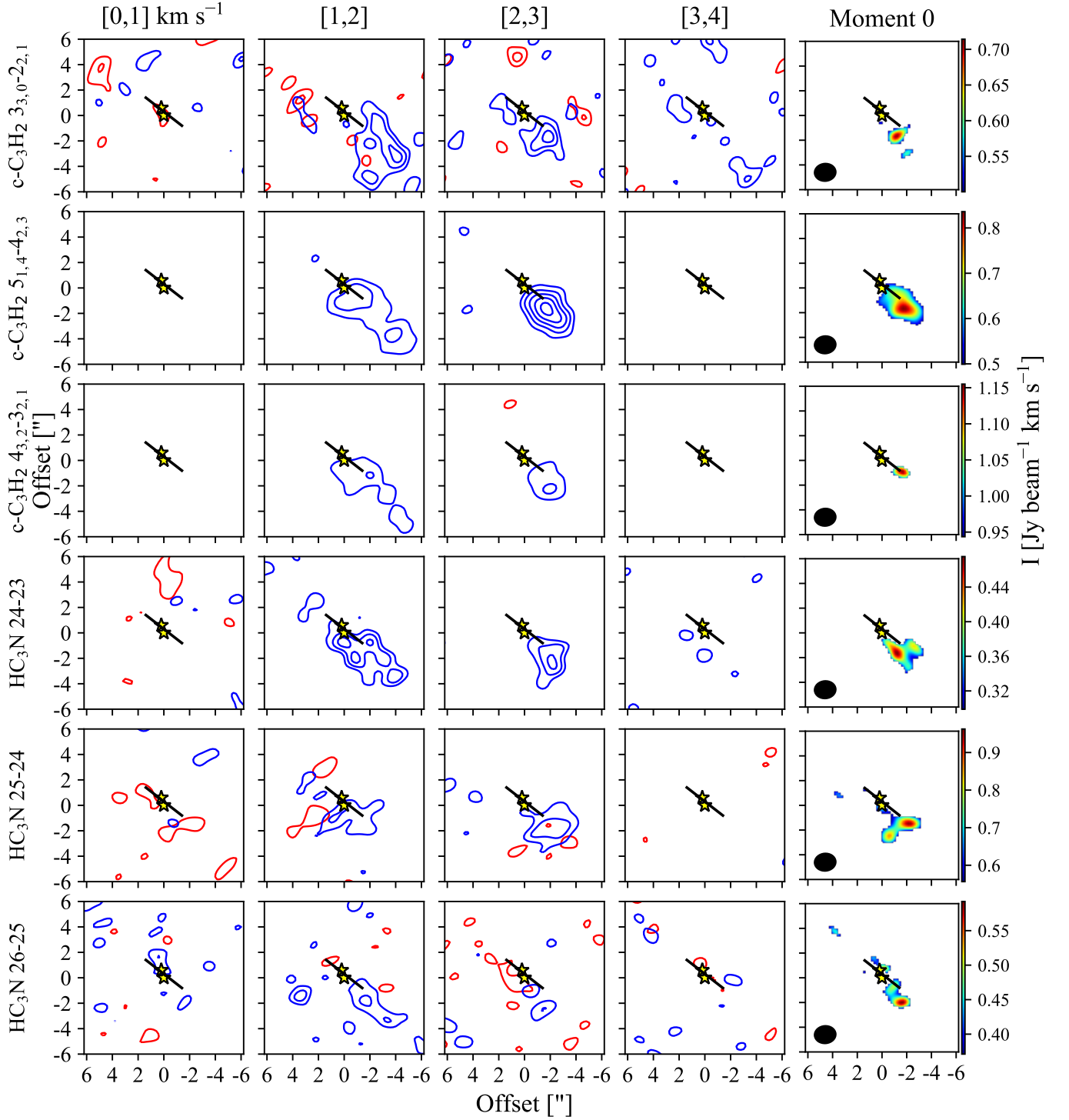


Fig. A.3. Emission of $c\text{-C}_3\text{H}_2$ and HC_3N . Channel maps consist of velocity ranges of 1 km s^{-1} and moment 0 maps are integrated over a velocity range of 8 km s^{-1} . The contours start at 3σ and follow a step of 3σ and 2σ for $c\text{-C}_3\text{H}_2$ and HC_3N , respectively. The yellow stars show the position of the sources and the solid segment represents the extent of the circumbinary disc. The synthesised beam is represented by a black filled ellipse in the right panels.

Table B.1. Parameters of the non-detected molecular transitions.

Species	Transition	Frequency ^(a) (GHz)	A_{ij} ^(a) (s ⁻¹)	E_u ^(a) (K)	n_{crit} ^(b) (cm ⁻³)
CO- species					
p-H ₂ CO	11 _{2,9} –12 _{0,12}	215.97616	3.16×10^{-7}	280	3.3×10^4
o-H ₂ CO	9 _{1,8} –9 _{1,9}	216.56865	7.24×10^{-6}	174	2.1×10^5
CH ₃ OH	5 _{0,5} –4 _{0,4}	241.70022	6.03×10^{-5}	48	1.7×10^6
CH ₃ OH	5 _{0,5} –4 _{0,4} ⁺⁺	241.79143	6.03×10^{-5}	35	4.6×10^5
CH ₃ OH	5 _{1,4} –4 _{1,3}	241.87907	6.03×10^{-5}	56	1.5×10^7
CH ₃ OH	5 _{1,4} –4 _{1,3} ⁻⁻	241.91583	6.03×10^{-5}	50	5.5×10^7
S- species					
SO	1 ₂ –2 ₁	236.45229	1.41×10^{-6}	16	4.0×10^4 ^(c)
SO ₂	11 _{1,11} –10 _{0,10}	221.96522	1.15×10^{-4}	60	8.6×10^6 ^(d)
SO ₂	12 _{3,9} –12 _{2,10}	237.06883	1.15×10^{-4}	60	1.1×10^8 ^(d)
SO ₂	5 _{2,4} –4 _{1,3}	241.61580	8.51×10^{-5}	24	9.4×10^6 ^(d)
SO ₂	14 _{0,14} –13 _{1,13}	244.25422	1.62×10^{-4}	94	1.2×10^7 ^(d)
OCS	$J=18$ –17	218.90336	3.02×10^{-5}	100	8.2×10^5
OCS	$J=19$ –18	231.06099	3.55×10^{-5}	111	1.3×10^6
OCS	$J=20$ –19	243.21804	4.17×10^{-5}	123	3.5×10^5
p-H ₂ S	2 _{2,0} –2 _{1,1}	216.71044	4.90×10^{-5}	84	1.1×10^6
HCS	6 _{0,6} –5 _{0,5}	241.68929	1.20×10^{-5}	41	
HSC	6 _{1,6} –5 _{1,5}	239.05112	4.27×10^{-4}	53	
HSC	6 _{2,5} –5 _{2,4}	243.32134	4.17×10^{-4}	94	
HSC	6 _{0,6} –5 _{0,5}	243.36604	4.68×10^{-4}	41	
HSC	6 _{2,4} –5 _{2,3}	243.52763	4.17×10^{-4}	94	
H ₂ CS	7 _{1,7} –6 _{1,6}	236.72702	1.91×10^{-4}	59	5.5×10^6
H ₂ CS	7 _{0,7} –6 _{0,6}	240.26687	2.04×10^{-4}	46	2.0×10^7
H ₂ CS	7 _{2,6} –6 _{2,5}	240.38205	1.91×10^{-4}	99	4.0×10^6
H ₂ CS	7 _{2,5} –6 _{2,4}	240.54907	1.91×10^{-4}	99	6.4×10^6
H ₂ CS	7 _{1,6} –6 _{1,5}	244.04850	2.09×10^{-4}	60	4.1×10^6
Carbon-chain species					
N ₂ D ⁺	3–2	231.32186	7.08×10^{-4}	22	2.1×10^6 ^(e)
H ₂ CN	3 _{0,3} –2 _{0,2}	219.85186	3.39×10^{-4}	21	
H ₂ CN	3 _{1,2} –2 _{1,1}	227.43700	3.39×10^{-4}	34	
c-C ₃ H ₂	8 _{2,6} –8 _{1,7} (para)	218.44883	1.48×10^{-4}	87	6.7×10^7
c-C ₃ H ₂	8 _{3,6} –8 _{2,7} (ortho)	218.44944	1.48×10^{-4}	87	3.2×10^8
c-C ₃ H ₂	3 _{2,1} –2 _{1,2} (ortho)	244.22215	5.89×10^{-5}	18	1.2×10^7
l-C ₃ H ₂	11 _{1,11} –10 _{1,10}	226.54857	1.07×10^{-3}	79	
l-C ₃ H ₂	11 _{0,11} –10 _{0,10}	228.60835	1.12×10^{-3}	66	
l-C ₃ H ₂	11 _{1,10} –10 _{1,9}	230.77801	1.15×10^{-3}	80	
C ₄ H	$N=23$ –22, $J=47/2$ –45/2	218.83701	4.47×10^{-5}	126	
C ₄ H	$N=23$ –22, $J=45/2$ –43/2	218.87537	4.47×10^{-5}	126	
C ₄ H	$N=24$ –23, $J=49/2$ –47/2	228.34862	5.13×10^{-5}	137	
C ₄ H	$N=24$ –23, $J=47/2$ –45/2	228.38696	5.13×10^{-5}	137	
C ₄ H	$N=25$ –24, $J=51/2$ –49/2	237.85974	5.75×10^{-5}	148	
C ₄ H	$N=25$ –24, $J=49/2$ –47/2	237.89806	5.75×10^{-5}	148	
Others					
SiO	$J=5$ –4	217.10498	5.25×10^{-4}	31	2.2×10^7
HDO	3 _{1,2} –2 _{2,1}	225.89672	1.32×10^{-5}	167	7.3×10^6
HDO	2 _{1,1} –2 _{1,2}	241.56155	1.17×10^{-5}	95	9.6×10^5
HNCO	10 _{0,10} –9 _{0,9}	219.79827	1.48×10^{-4}	58	4.4×10^8
HNCO	11 _{0,11} –10 _{0,10}	241.77403	1.95×10^{-4}	70	2.3×10^7

Notes. ^(a) Values from the CDMS database (Müller et al. 2001). ^(b) Calculated values for a collisional temperature of 30 K and collisional rates from the Leiden Atomic and Molecular Database (LAMDA; Schöier et al. 2005). ^(c) For a collisional temperature of 60 K. ^(d) For a collisional temperature of 100 K. ^(e) Calculated for N₂H⁺. The collisional rates of specific species listed here and in Table 3 were taken from the following sources: CO isotopologues from Yang et al. (2010), H₂CO and H₂CS from Wiesenfeld & Faure (2013), CH₃OH from Rabli & Flower (2010), DCO⁺ and N₂D⁺ from Flower (1999), DCN and DNC from Dumouchel et al. (2010), CS isotopologues and SO from Lique et al. (2006), SO₂ from Balança et al. (2016), OCS from Green & Chapman (1978), H₂S from Daniel et al. (2011), CN from Kalugina & Lique (2015), C₃H₂ from Chandra & Kegel (2000), HC₃N from Faure et al. (2016), SiO from Dayou & Balança (2006), HDO from Faure et al. (2012), and HNCO from Sahnoun et al. (2018).

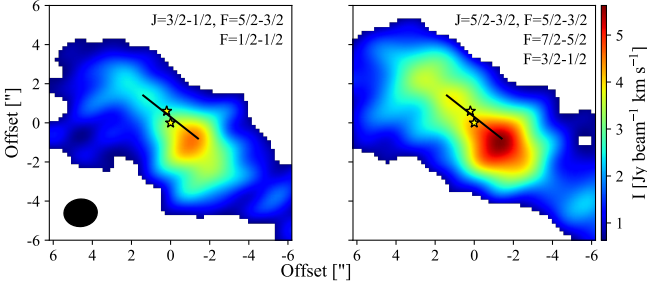


Fig. A.4. CN moment 0 maps of the brightest transitions, which are blended with other hyperfine lines. The integration is done over a velocity range of 11 and 8 km s⁻¹ for the left and right panels, respectively. The yellow stars show the position of the sources and the solid segment represents the extent of the circumbinary disc. The synthesised beam is represented by a black filled ellipse in the left panel.

Table C.1. Comparison between APEX (Lindberg et al. 2017) and convolved SMA intensities.

Molecular transition	Intensity (K km s ⁻¹)		Filtering (%) ^(a)
	APEX	SMA	
DCO ⁺ $J=3-2$	0.317	0.0125	96
c-C ₃ H ₂ $6_{0,6}-5_{1,5}$	0.177	0.0137	92
p-H ₂ CO $3_{0,3}-2_{0,2}$	0.431	0.0036	99
C ¹⁸ O $J=2-1$	3.198	0.0093	> 99
SO 6_5-5_4	0.316	0.0003	> 99

Notes. ^(a) Percentage of the emission filtered-out by the interferometer.

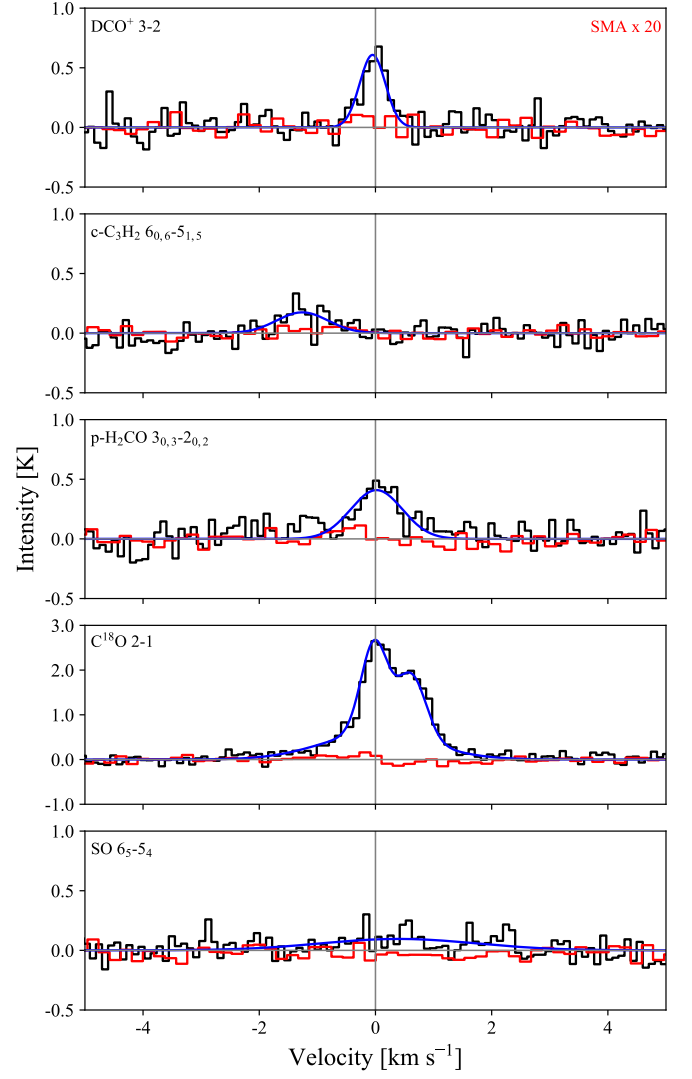


Fig. C.1. Spectra from APEX data (black) and convolved SMA data with a 29'' beam (red). For clarity, the SMA spectra are scaled with a factor of 20. The blue curve represents a Gaussian fit and, for C¹⁸O, the curve shows the sum of three Gaussian components.